Materials Science and Engineering A 537 (2012) 11–24

Contents lists available at SciVerse ScienceDirect

Materials Science and Engineering A

journal homepage: www.elsevier.com/locate/msea

Microstructure and mechanical properties of weld-bonded and resistance spot welded magnesium-to-steel dissimilar joints

W. Xu [a], D.L. Chen [a,*], L. Liu [b], H. Mori [b,1], Y. Zhou [b]

[a] Department of Mechanical and Industrial Engineering, Ryerson University, 350 Victoria Street, Toronto, Ontario M5B 2K3, Canada
[b] Department of Mechanical and Mechatronics Engineering, University of Waterloo, 200 University Avenue West, Waterloo, Ontario N2L 3G1, Canada

ARTICLE INFO

Article history:
Received 4 October 2011
Received in revised form
29 November 2011
Accepted 20 December 2011
Available online 17 January 2012

Keywords:
Weld-bonding
Resistant spot welding
AZ31B-H24 magnesium alloy
HSLA steel
Dissimilar joint
Mechanical properties

ABSTRACT

The aim of this study was to evaluate microstructures, tensile and fatigue properties of weld-bonded (WB) magnesium-to-magnesium (Mg/Mg) similar joints and magnesium-to-steel (Mg/steel) dissimilar joints, in comparison with resistance spot welded (RSW) Mg/steel dissimilar joints. In the WB Mg/Mg joints, equiaxed dendritic and divorced eutectic structures formed in the fusion zone (FZ). In the dissimilar joints of RSW and WB Mg/steel, FZ appeared only at Mg side with equiaxed and columnar dendrites. At steel side no microstructure changed in the WB Mg/steel joints, while the microstructure in the RSW Mg/steel joints consisted of lath martensite, bainite, pearlite and retained austenite leading to an increased microhardness. The relatively low cooling rate suppressed the formation of shrinkage porosity but promoted the formation of $MgZn_2$ and Mg_7Zn_3 in the WB Mg/steel joints. The added adhesive layer diminished stress concentration around the weld nugget. Both WB Mg/Mg and Mg/steel joints were significantly stronger than RSW Mg/steel joints in terms of the maximum tensile shear load and energy absorption, which also increased with increasing strain rate. Fatigue strength was three-fold higher for WB Mg/Mg and Mg/steel joints than for RSW Mg/steel joints. Fatigue failure in the RSW Mg/steel joints occurred from the heat-affected zone near the notch root at lower load levels, and in the mode of interfacial fracture at higher load levels, while it occurred in the Mg base metal at a maximum cyclic load up to ~10 kN in both WB Mg/Mg and Mg/steel joints.

1. Introduction

Due to huge concerns on the global warming caused by recently recognized man-made greenhouse gas emissions and rising energy prices, demands for environmental-friendly transportation vehicles with better fuel efficiency and reduction of atmospheric pollution have received considerable attention [1–5]. To achieve such goals and meet legislative regulations, manufacturers in the automotive and aerospace sectors have to count on reducing the vehicle weight via applying advanced lightweight materials and innovative joining techniques [6–9].

Recently, the development and application of ultralight-weight magnesium alloys have been significantly increasing in the transportation sectors due to their low density, high strength-to-weight ratio, and superior damping capacity [10–15]. On the other hand, high strength low alloy (HSLA) steels have been widely acceptable for years by automotive manufacturers due to their excellent combination of strength with formability and fitness for assembly [16,17]. The growing applications of lightweight magnesium alloys have to involve the dissimilar joining between magnesium alloys and steels. Therefore, it is important to develop the joining technology of Mg alloys with HSLA steels.

Weld-bonding (WB) which combines resistance spot welding (RSW) with adhesive-bonding, originally developed to prevent noise and vibrations for aircraft, automobile production and railway carriages, is an innovative and advanced hybrid joining technology since it has the advantages of both RSW and adhesive bonding, including reduced manufacturing costs, superior static and fatigue properties, improved corrosion resistance [18–23]. While RSW alone has been extensively used in the automobile manufacturing (e.g., about 90% assembly work is done with RSW in a typical auto body, with about 7000–12,000 spot welds depending on the size of vehicle [24]), there is a tendency of using adhesive bonding to replace RSW since the first application of precision robot-dispensed two-part adhesives for bonding body-in-white structure [25]. Indeed, it has been reported that automotive manufacturers such as Audi, VW, Peugeot Renault, Volvo, and BL have an active interest in bonding as a process to replace RSW in their product since 1980s [26].

* Corresponding author. Tel.: +1 416 979 5000x6487; fax: +1 416 979 5265.
E-mail address: dchen@ryerson.ca (D.L. Chen).
[1] Permanent address: Department of Management of Industry and Technology, Osaka University, 2-1 Yamadaoka, Suita, Osaka 565-0871, Japan.

0921-5093/$ – see front matter © 2011 Elsevier B.V. All rights reserved.
doi:10.1016/j.msea.2011.12.096

Table 1
Chemical composition of AZ31B-H24 Mg alloy.

Element	Al	Zn	Mn	Si	Fe	Mg
Content (wt.%)	2.92	1.09	0.3	0.01	–	Balance

A new attempt of WB Mg-to-Mg and Mg-to-steel could bring benefits of vehicle weight reduction due to the combination of new WB joining technique with strategic ultralight-weight magnesium alloys. However, the integrity and durability of WB Mg/Mg similar welds and Mg/steel dissimilar welds especially under cyclic loading are unknown, since no fatigue behavior of such welds in relation to the microstructural changes has been reported in the literature. It is unclear how big difference there would be between WB and RSW joints when a magnesium alloy is involved. The main objective of the present study was, therefore, to identify the influence of adhesive addition on the microstructures, tensile and fatigue properties of similar WB Mg/Mg and dissimilar Mg/steel joints.

2. Materials and experimental procedure

The materials used in the present study were AZ31B-H24 Mg alloy sheet and hot-dip galvanized HSLA steel sheet, with a thickness of 2.0 mm and 0.7 mm, respectively. The chemical compositions for the AZ31B Mg alloy and HSLA steel are shown in Tables 1 and 2. The test coupons of 25 mm in width and 100 mm in length were cut. Specimens were ultrasonically cleaned for 5 min in acetone. Prior to welding the surfaces of Mg coupons were further cleaned with a solution of 2.5% (w/v) chromic acid to remove surface oxides. For WB, Terokal® 5087-02P adhesive had been applied and then cured at a temperature of 180 °C for 30 min. The welding parameters were selected to be 8 kA, 3 cycles plus 24 kA, 8 cycles using alternate current (AC) for WB Mg/Mg (*weld-bonded AZ31 to AZ31 Mg alloy*) joints; 8 kA, 3 cycles plus 24 kA, 8 cycles using direct current (DC) for WB Mg/steel (*weld-bonded AZ31 Mg alloy to HSLA steel*) joints; and 28 kA, 8 cycles with DC for RSW Mg/steel (*resistance spot welded AZ31 Mg alloy to HSLA steel*) joints. Symmetrical electrode cap (FF25) with a sphere radius of 50.8 mm and a face diameter of 16 mm was used for WB Mg/Mg similar welding. Asymmetrical electrodes, with a FF25 electrode cap against Mg side and a flat face electrode against steel side, were used for both WB Mg/steel and RSW Mg/steel dissimilar welding, aiming to balance the workpiece heating by reducing current density and increasing cooling rate of the steel sheet.

The metallographic samples were sectioned across the weld center parallel to the loading direction, and then cold mounted, ground, polished and etched with a solution of 4.2 g picric acid, 10 ml acetic acid, 70 ml ethanol, and 10 ml water. An optical microscope in conjunction with Clemex image analysis system was used to observe the microstructures of weld nuggets and base metal. Vickers microhardness tests were performed on the unetched samples. A load of 200 g and a dwell time of 15 s were used during hardness testing. All indentations were adequately spaced to avoid any potential effect of strain fields caused by adjacent indentations. On the polished cross-sectional surface, the hardness test lines were inclined at about 6° to the faying surface and passed the joint center which was set to be 0 mm. Before all the microhardness tests, calibrations were conducted using a standard reference test block. Tensile tests were carried out at room temperature using a fully computerized United tensile testing machine at different crosshead speeds of 0.1 mm/min, 1.0 mm/min, and 10.0 mm/min for each group (WB Mg/Mg joints, WB Mg/steel joints, and RSW Mg/steel joints). Two samples were tested at each crosshead speed. Fatigue tests were performed using a fully computerized Instron 8801 servo-hydraulic testing system under load control at different maximum loads. A load ratio of R (P_{min}/P_{max}) equal to 0.2, sinusoidal waveform, and frequency of 50 Hz were used in all the tests. Two samples were tested at each load level chosen. The fracture surface morphology and microstructures were examined using a JSM-6380LV scanning electron microscope (SEM) equipped with Oxford energy dispersive X-ray spectroscopy (EDS) system and 3D fractographic analysis capacity. Furthermore, a multi-functional PANalytical X-ray diffractometer was used to identify the formation of potential intermetallic compounds after Mg/steel dissimilar welding from the fracture surface (Mg side) after tensile tests. X-ray diffraction (XRD) was performed using CuK_α radiation at 45 kV and 40 mA. The diffraction angle (2θ) at which the X-rays hit the sample varied from 20° to 90° with a step size of 0.05° and 3 s in each step.

Table 2
Chemical composition of HSLA steel.

Element	C	Si	Mn	P	S	Ni
Content (wt.%)	0.060	0.227	0.624	0.006	0.004	0.013
Element	Cr	Mo	Cu	Al	Ti	Nb
Content (wt.%)	0.041	0.005	0.044	0.039	0.003	0.021

3. Results and discussion

3.1. Microstructure

The overall joint nugget and microstructural changes across a WB Mg/Mg joint are shown in Fig. 1. It is seen that the cross-section of the weld (Fig. 1(a)) exhibited a big microstructural change. At or near the fusion center (Fig. 1(b and c)) the microstructure consisted of equiaxed dendrites containing divorced eutectic $Mg_{17}Al_{12}$ particles [27–29] mainly located at the interdendritic and intergranular regions. Similar microstructure in the FZ center of AZ31B-H24 Mg alloy after laser welding or double-sided arc welding has been reported in Refs. [30,31]. Comparing Fig. 1(c) with (b) it appeared that the dendrite cell size (or grain size) became smaller with increasing distance from the FZ center. Near the FZ border the divorced eutectic $Mg_{17}Al_{12}$ particles were mainly located at the boundaries of less obvious dendrite grains which became further smaller (Fig. 1(d)). The microstructural change in the FZ border area can be seen in Fig. 1(e), where no divorced eutectic $Mg_{17}Al_{12}$ particles in the HAZ were present. This can be better seen on the image taken in the HAZ (Fig. 1(f)). Fig. 1(g) shows the microstructure in the base metal (BM) which consisted of deformed and elongated grains, similar to that reported in Refs. [30,31]. Even though the grain size (or dendrite cell size) decreased with increasing distance from the FZ center, it was still larger than that of BM, as seen from Fig. 1(b–f) versus (g).

Furthermore, it was observed from Fig. 1(c–e) that no columnar dendritic structure near the FZ border was developed in the WB Mg/Mg joint. Similar observations of no or undeveloped columnar dendritic structure were also reported in the resistance spot welding by Wang et al. [14] on 1 mm thick AZ31B-H24 Mg alloy sheets, and by Xiao et al. [32] and Liu et al. [33] on the hot-rolled sheets of AZ31 Mg alloy. This was related to the columnar-to-equiaxed transition influenced by second-phase particles in the fusion pool during welding. According to Burden and Hunt [34], the columnar-to-equiaxed transition during nugget solidification occurred either by a pile-up of equiaxed crystals that blocked the growth of columnar grains or by the attachment of equiaxed crystals from the liquid to the columnar dendrite front. Xiao et al. [32] have recently observed that during solidification of the fusion pool, when the size of the second-phase particles in front of the interface was large

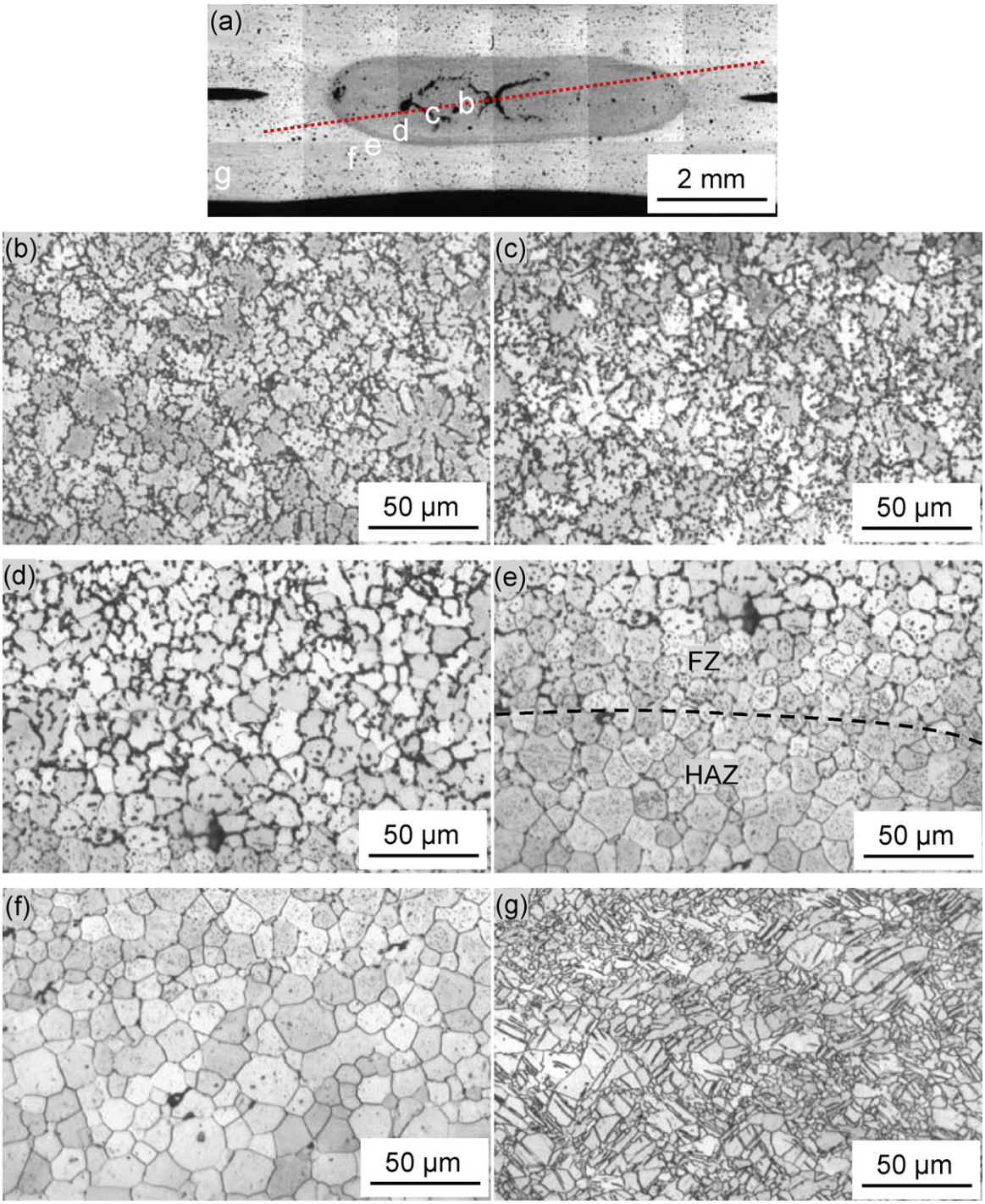

Fig. 1. Microstructures of a WB Mg/Mg joint: (a) overall view of nugget where the location of the subsequent images is indicated, (b) and (c) equiaxed dendritic structure at and near the center of FZ with divorced eutectic $Mg_{17}Al_{12}$ particles, (d) microstructure near the FZ border, (e) FZ/HAZ border area, (f) HAZ, and (g) base metal (BM).

enough, new grains would nucleate and grow in the areas near the FZ boundary and these coarser second-phase particles would block off the epitaxial columnar grains. As a result, columnar dendritic grain growth would be restricted, and equiaxed grains developed, as seen in Fig. 1(d and e).

Kou [35] presented a constitutional supercooling theory associated with the ratio of temperature gradient (G) to growth rate (R). When G/R ratio is very low, the region of constitutional supercooling is so wide that solid nuclei form in front of the advancing solid/liquid interface and grow into equiaxed dendrites as solidification proceeds. Similar situation was observed by Liu et al. [33] who reported that when the welding current increased from 22 kA to 26 kA during RSW of Mg/Mg, the columnar dendritic zone (CDZ) near the FZ border became smaller; when the welding current further increased from 26 kA to 28 kA, the CDZ disappeared. Since the higher welding current gave rise to a higher heat input, leading to a lower temperature gradient and a higher cooling rate which promoted the columnar-to-equiaxed transition. The absence of the columnar structure near the FZ border in the present WB Mg/Mg joint was basically due to more heat generation and higher temperature due to the presence of adhesive added (Fig. 2, as reported by [36]). Then the temperature gradient would become lower,

Fig. 2. A macroscopic image of a typical fatigue fracture surface of the WB Mg/Mg joint, showing the retained adhesive layer and the central fusion zone where the adhesive was squeezed or burned off.

resulting in a low G/R ratio and promoting the columnar-to-equiaxed grain transition.

From Fig. 1(a) it is also seen that in the WB Mg/Mg joint, solidification or shrinkage cracking occurred. The formation of solidification cracking was basically due to the presence of low melting point liquid films between dendrites due to the segregation of Al and Mn atoms and tensile stress developed during cooling [37,38]. The shrinkage porosity and cavities in the FZ of a given metal were closely related to its thermal expansion in the welding process and forge force at the later stage of welding [39]. Since AZ31 Mg had a relatively high coefficient of volume expansion in liquid at its melting point ($1.65 \times 10^{-4}\,K^{-1}$), in comparison with that of aluminum ($1.31 \times 10^{-4}\,K^{-1}$) or iron ($0.89 \times 10^{-4}\,K^{-1}$), a higher tendency of forming shrinkage porosity and cavities than aluminum or iron would be expected in the fusion welding of Mg/Mg [40].

Figs. 3 and 4 show the microstructures of WB Mg/steel joint and RSW Mg/steel joint, respectively. At the Mg side, both samples had a similar microstructure consisting of four zones, namely, (i) equiaxed dendritic zone in the FZ of Mg alloy close to HSLA in Figs. 3(b) and 4(b), (ii) columnar dendritic zone in Figs. 3(d) and 4(d), (iii) HAZ at the top of Figs. 3(e) and 4(e), and (iv) BM of AZ31 Mg alloy like Fig. 1(g), where Figs. 3(c) and 4(c) show the border area between the equiaxed dendritic zone and columnar dendritic zone. It is seen from Fig. 4(b) that the Mg FZ adjacent to the HSLA showed some clear shrinkage cracks or cavities in the RSW Mg/steel joint without adhesive, while such shrinkage cracks were basically absent in the WB Mg/steel joint with the addition of adhesive (Fig. 3(b)). This would be due to a lower cooling rate in the WB Mg/steel process than in the RSW Mg/steel process. The heat input during resistance spot welding could be expressed by the following equation according to Joule's law [41],

$$Q = I^2Rt = I^2 \int_0^t R(t)dt, \tag{1}$$

where Q is the heat energy in J, I is the welding current in A, t is the welding time in s, and R is the dynamic resistance in ohm as a function of welding time t. It is clear that both welding current and dynamic resistance can affect the heat generation. However, the welding current has a much stronger effect on the heat generation than the dynamic resistance, i.e., a square dependence versus a linear dependence. While the adhesive added could increase the dynamic resistance [36], greater heat generation and higher peak temperature would still be achieved in the present RSW Mg/steel joint, because the constant DC welding current in the RSW Mg/steel process (28 kA, 8 cycles) was higher than that in the WB Mg/steel process (24 kA, 8 cycles with only a slight preheating at 8 kA, 3 cycles). The higher peak temperature in the RSW Mg/steel process would give rise to a faster cooling rate in terms of the thermal theory of convection transfer (sometimes called the Newton's law of cooling) [42,43],

$$\dot{Q} = hA(T_{env} - T(t)) = -hA\,\Delta T(t), \tag{2}$$

where $\dot{Q}$ is the change of thermal energy Q with respect to time t (i.e., dQ/dt), h is the heat transfer coefficient, A is the surface area of the heat being transferred, T is the object's surface temperature, T_{env} is the temperature of the environment. Obviously, the rate of heat loss of a body is proportional to the temperature difference between the body and its surroundings. This has indeed been verified via direct measurements during welding of different materials [7,44,45]. Therefore, a faster cooling rate in the RSW Mg/steel process would be anticipated due to the higher welding current (or heat energy) applied, in comparison with the WB Mg/steel process.

There were essentially no changes in the microstructure at the steel side in WB Mg/steel process with the addition of adhesive due to a slower cooling rate as shown in Fig. 3(f and g) where only ferrite was present in the HAZ. However, in the RSW Mg/steel joint without using any adhesive and with a higher cooling rate, the microstructural change in the HAZ of HSLA occurred to form mainly lath martensite, as compared in Fig. 4(f) with (g). Such a change could be better seen in Fig. 5, where more detailed observations in the areas of "h", "i", and "j" indicated in Fig. 4(f) via SEM at a higher magnification are presented. As reported in Refs. [46,47], the fast cooling rate during RSW of HSLA could lead to the formation of martensite, bainite, pearlite and some retained austenite, depending on the cooling rate, peak temperature, alloying element, etc. Similar studies [48,49] on martensite in a HSLA steel have also indicated that the cooling rates during RSW were very high, which gave an insufficient time for the diffusion of carbon and other alloying elements, leading to the formation of lath martensite containing very thin regions of retained austenite between the laths, or pockets of laths, and possibly some lower bainite, pearlite and some carbides.

It is of interest to observe that nearly no microstructural change in the HAZ of HSLA occurred within approximately 0.1 mm from

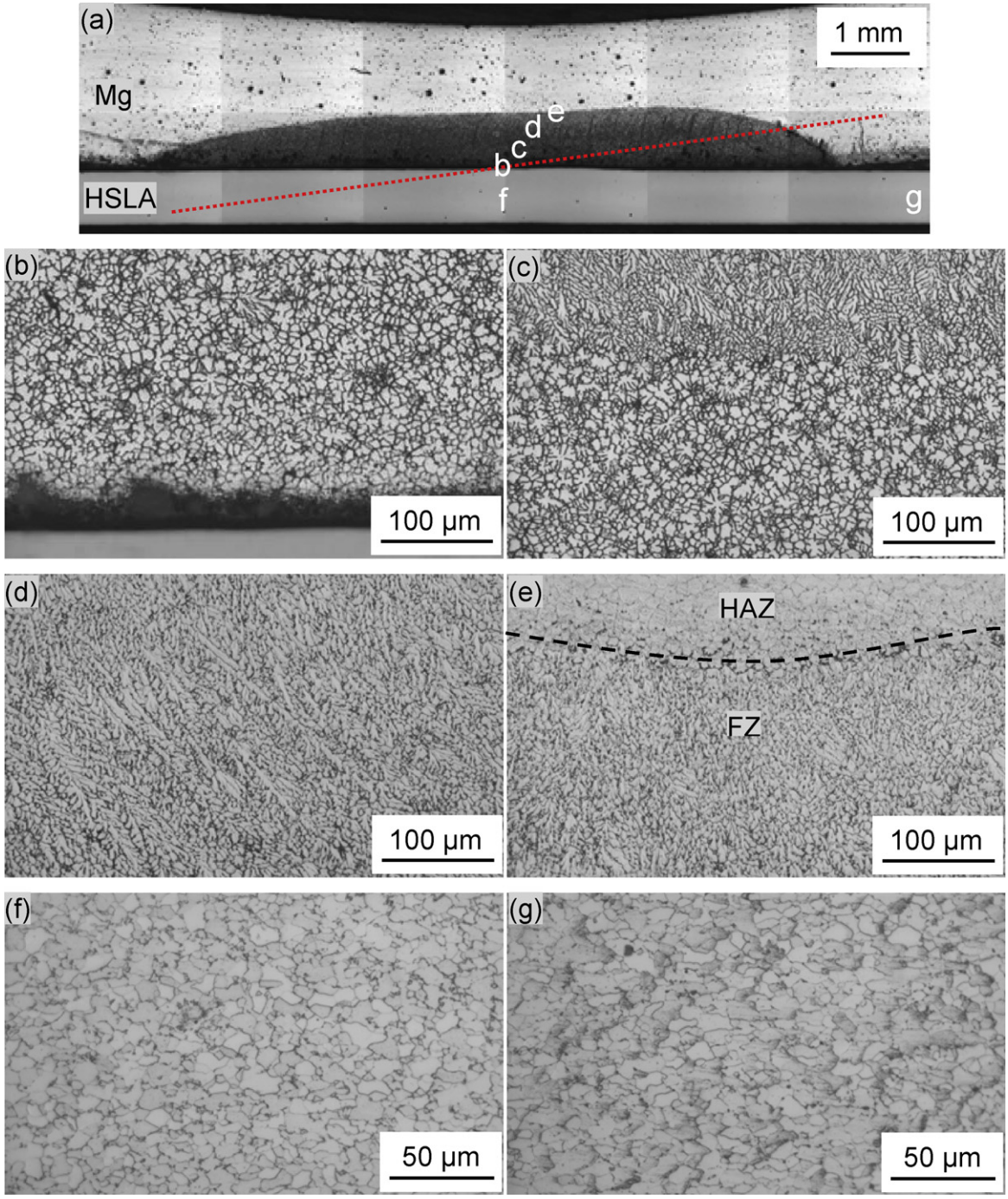

Fig. 3. Microstructures of a WB Mg/steel joint: (a) overall view of nugget where the location of the subsequent images is indicated, (b) equiaxed dendritic structure in the FZ of Mg alloy near HSLA, (c) border area between the equiaxed and columnar dendritic structures, (d) columnar dendritic structure, (e) FZ/HAZ border area, (f) HAZ of HSLA side, and (g) BM of HSLA sheet.

the edge bordering the magnesium (Fig. 4(f)). This could be understood as follows. The heat generation in both steel and magnesium sheets was unequal, which would be higher at the steel side than at the magnesium side because the electrical conductivity of steel was lower than that of magnesium [41,50]. The steel could then serve as a hot anvil to heat the magnesium. Because of the heat losses from both sides of magnesium and steel/electrode with circulating cooling water, only in the center portion of the steel sheet the peak temperature experienced could reach above the austenization temperature (but below the melting point, as indicated by the absence of fusion zone at the HSLA side). The subsequent rapid cooling led to the formation of martensite alongside some bainite, pearlite, and retained austenite. The presence of the ~0.1 mm non-transformation zone near the interface (Figs. 4(f) and 5(a)) indicated that the peak temperature experienced in this area was below the austenization temperature. This might be related to a lower melting temperature of ~630 °C for AZ31 Mg alloy, which was below the austenization temperature of HSLA. In addition, heat loss or transfer at the magnesium side would be faster since magnesium had a higher thermal conductivity than steel (i.e., 96 W/(m K) [14] for magnesium versus 27 W/(m K) [51] for steel). It follows that the heat loss in the area at the steel side adjoining Mg sheet would also

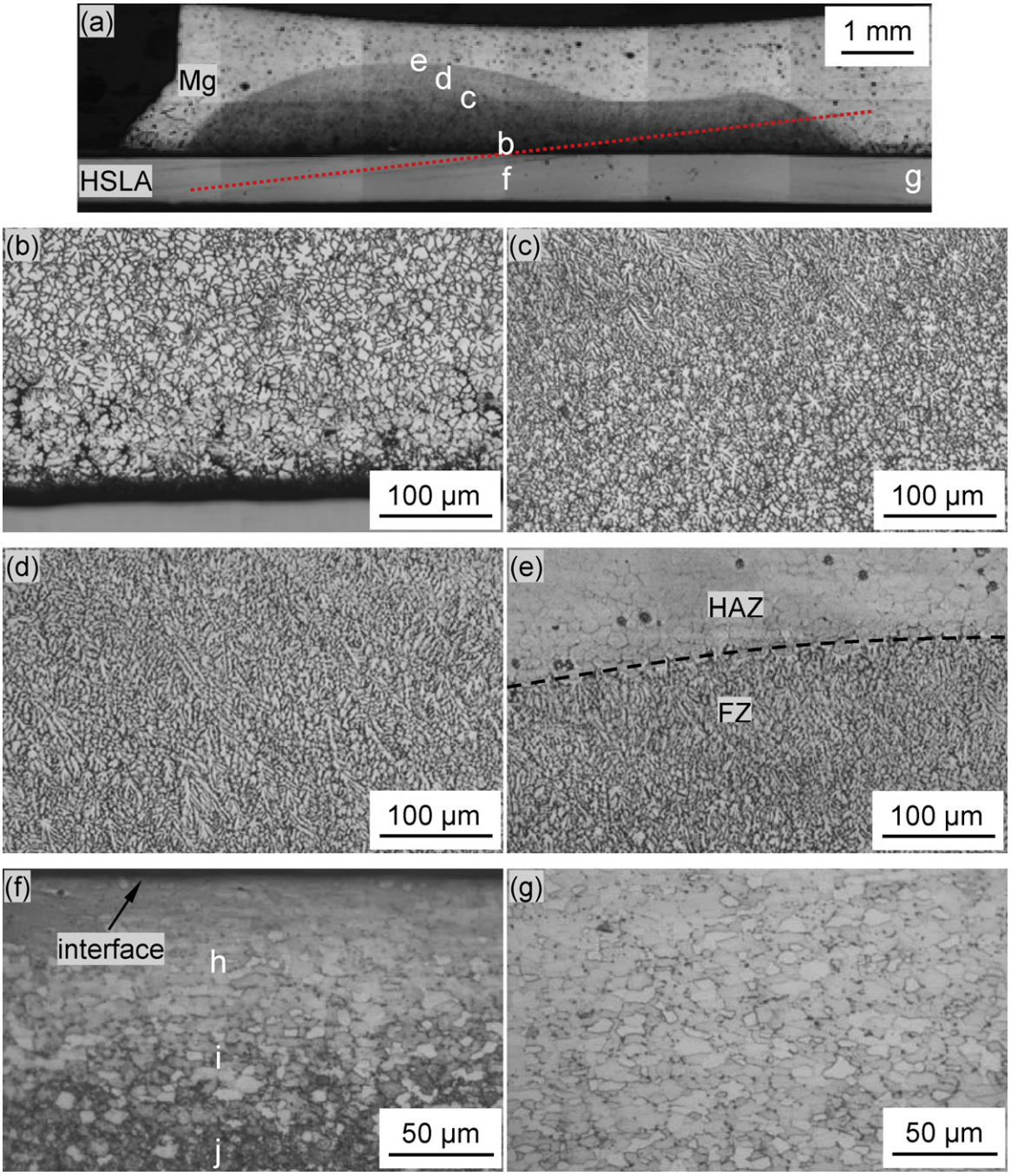

Fig. 4. Microstructures of a RSW Mg/steel joint: (a) overall view of nugget where the location of the subsequent images is indicated, (b) equiaxed dendritic structure in the FZ of Mg alloy close to HSLA, (c) border area between the equiaxed and columnar dendritic structures, (d) columnar dendritic structure, (e) FZ/HAZ border area, (f) HAZ of HSLA side, and (g) BM of HSLA sheet.

be faster, leading to a lower peak temperature below the austenization temperature and the absence of martensite (Figs. 4(f) and 5(a)). In the WB Mg/steel joint, as discussed above, the lower cooling rate prevented the formation of martensite in the HAZ of HSLA (Fig. 3(f)), in comparison with the RSW Mg/steel joint (Fig. 4(f)).

3.2. XRD analysis

XRD analyses were performed on the fracture surface (Mg side) of WB Mg/steel and RSW Mg/steel joints after tensile tests and the obtained results are shown in Fig. 6. For each sample, the nugget zone (or FZ) and BM were chosen for XRD scanning. Basically, Mg peaks appeared in the AZ31-H24 BM (Fig. 6(a)), while Zn-containing intermetallic compounds were detected on the fracture surface (Fig. 6(b and c)) since the HSLA was Zn-coated (hot-dip galvanized) sheet. Based on the binary Mg–Zn phase diagram [52,53], there are five possible intermetallic phases in the Mg–Zn system, namely Mg_7Zn_3, MgZn, Mg_2Zn_3, $MgZn_2$ and Mg_2Zn_{11}. Intermetallic compound (IMC) $MgZn_2$ (also reported in Refs. [54,55]) was observed on the fractured nugget zone of the RSW Mg/steel joint as shown in Fig. 6(b), while both $MgZn_2$ and Mg_7Zn_3 were detected on the fractured nugget zone of the WB Mg/steel joint (Fig. 6(c)). The Mg_7Zn_3 on the fracture surface of a WB Mg/steel joint could be seen from a typical back-scattered electron SEM image as shown in Fig. 7(a),

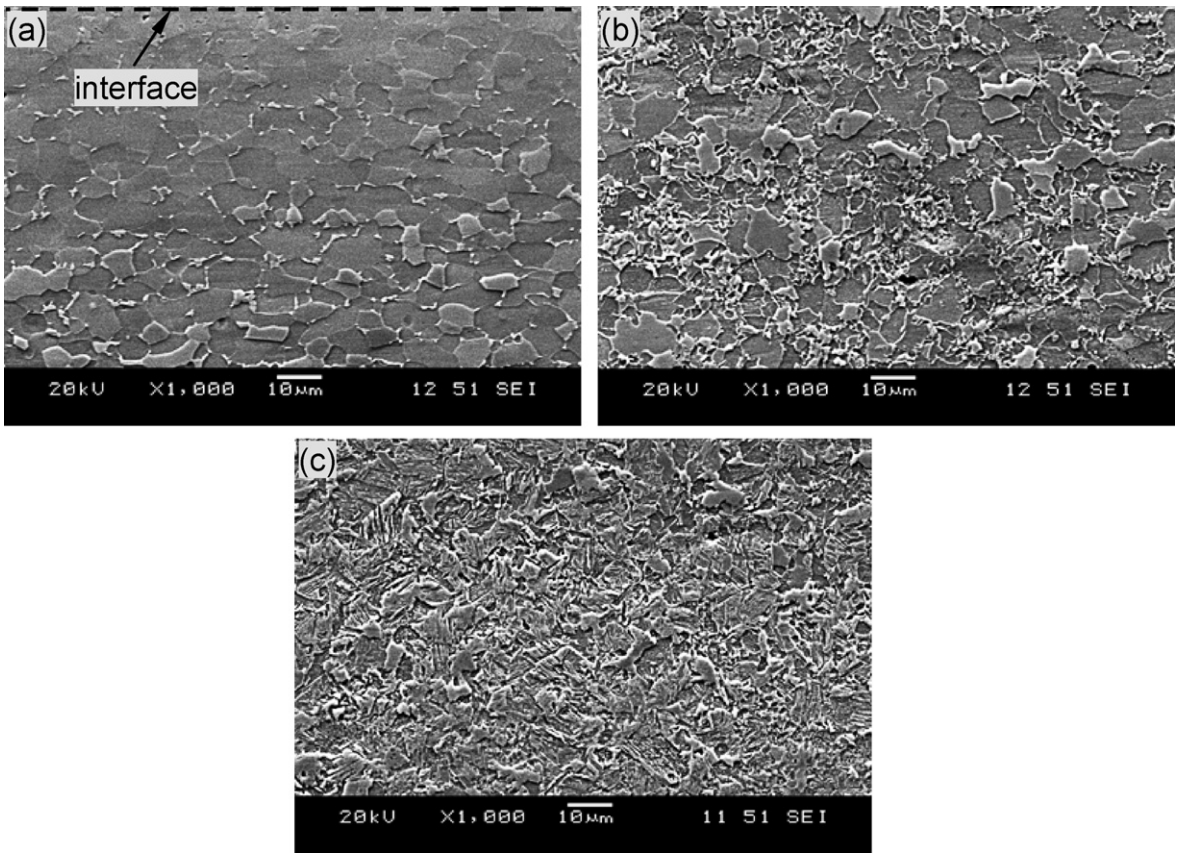

Fig. 5. SEM images showing the microstructural change at the steel side of the RSW Mg/steel joint in Fig. 3(f): (a) area h close to the interface, (b) area i, and (c) area j.

which was observed to be present discontinuously in the fusion zone at the WB Mg/steel joint interface. The corresponding energy dispersive X-ray spectroscopy (EDS) analysis (Fig. 7(b)) revealed an atom percent of 68% and 32% for elements Mg and Zn, respectively, which had an atom ratio close to that of Mg_7Zn_3, as detected by XRD (Fig. 6(c)). It should be noted that the C and O detected on the EDS spectrum were basically from the epoxy ($C_{21}H_{25}ClO_5$) based adhesive.

The formation of intermetallic compounds is known to be associated with the diffusion of participating atoms at high temperatures. Since diffusion is a time-dependent process, the formation of additional Mg_7Zn_3 compound was mainly attributed to the lower cooling rate in the WB Mg/steel process. It implied that a longer period of time at relatively higher temperatures would be experienced in the WB Mg/steel process, thus giving rise to enhanced diffusion and promoting the formation of Mg_7Zn_3 compound (Figs. 6(c) and 7). Similarly, Wu and Song [56] reported the presence of Mg_7Zn_3 compound in the fracture zone of brazed joints of AZ31B magnesium alloy, and Luo et al. [57] observed Mg_7Zn_3 compound present between quasicrystal phases in slowly cooled Mg–Zn–Y alloys. Further studies on the formation mechanisms of Mg_7Zn_3 compound in the WB Mg/steel joint are needed.

3.3. Hardness profiles

Vickers microhardness profiles across the weld nugget (as indicated by the dashed line in Figs. 1(a), 3(a) and 4(a)) were determined for the WB Mg/Mg similar joint, WB Mg/steel dissimilar joint, and RSW Mg/steel dissimilar joint, respectively, and the obtained results are plotted in Fig. 8. It is seen that in the WB Mg/Mg similar joint a nearly constant hardness value of ~HV60 across the FZ and HAZ was obtained. In the WB Mg/steel dissimilar joint, the Mg side had a similar hardness as that in the WB Mg/Mg similar joint, while the hardness at the steel side reached at an average of HV154, being equivalent to that of the BM. In the RSW Mg/steel dissimilar joint, the hardness of HAZ at steel side showed a gradual increase with increasing distance from the faying surface with a highest value of about HV225 and then decreased. This was obviously attributed to the change in the microstructure as shown in Figs. 4(f) and 5. Again, the hardness at the Mg side remained nearly constant at an average of about HV60 as well. For both RSW Mg/steel and WB Mg/steel dissimilar joints, an equivalent value of hardness near the interface between Mg and steel was obtained to be about HV110. Such a small plateau-like feature in both dissimilar joints was due to the presence of intermetallic compounds in the dissimilar welding (Fig. 6(b and c)) which resulted in an increase of hardness at the Mg side adjacent to the steel. Besides, the plateau-like feature was somewhat wider for the WB Mg/steel joint than for the RSW Mg/steel joint. This was likely due to the formation of both $MgZn_2$ and Mg_7Zn_3 intermetallic compounds (Figs. 6(c) and 7) during weld bonding, which led to a thicker layer of intermetallic compounds in the WB Mg/steel joint. In contrast, there was only $MgZn_2$ formed at the Mg side of RSW Mg/steel joint (Fig. 6(b)), thus bringing about a thinner layer intermetallic compound (Fig. 8).

3.4. Tensile properties

Typical curves of the applied load versus displacement under three welding conditions are shown in Fig. 9. It is seen that both WB joints were much stronger than RSW Mg/steel joint, while WB Mg/Mg joint was further stronger than WB Mg/steel joint. The evaluated maximum tensile shear load is shown in Fig. 10(a). It is clear that the maximum tensile shear load of the WB Mg/Mg joint was higher than that of the WB Mg/steel joint, which was

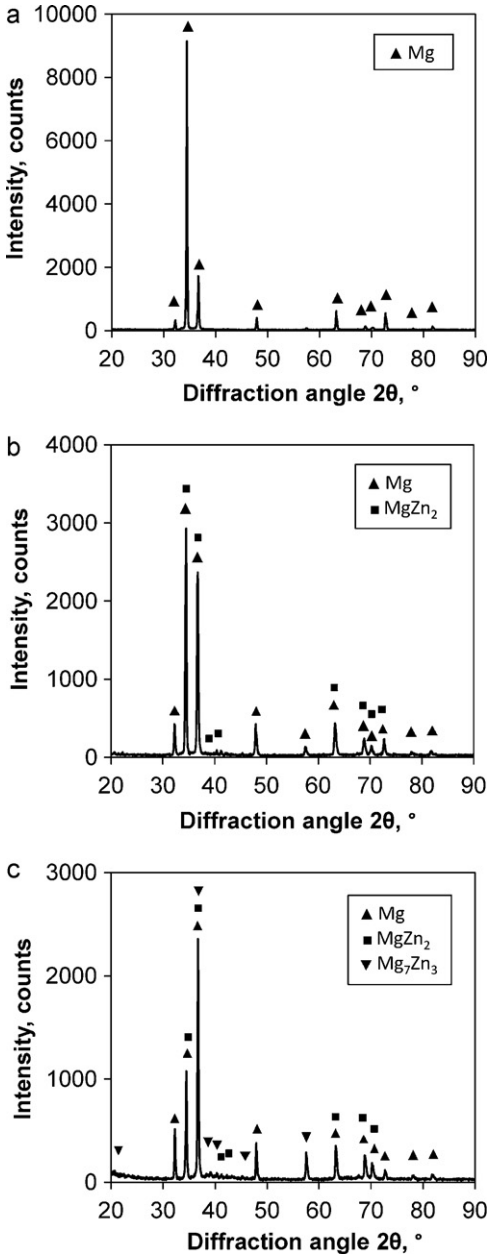

Fig. 6. XRD patterns obtained from the Mg side of fracture surfaces: (a) base metal, (b) RSW Mg/steel joint, and (c) WB Mg/steel joint.

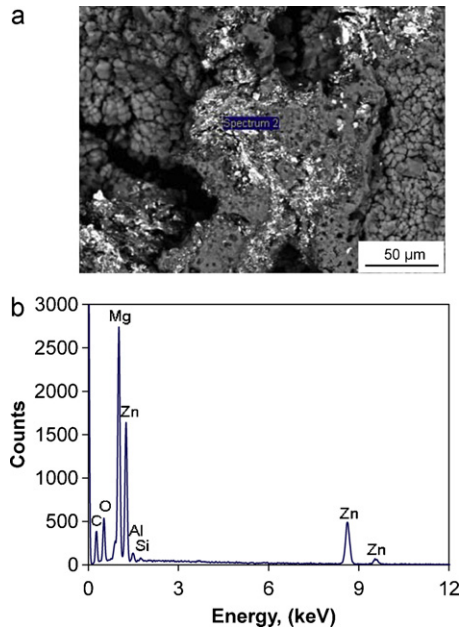

Fig. 7. (a) A typical SEM image showing Mg_7Zn_3 formed in the fusion zone at the WB Mg/steel joint interface and (b) EDS spectrum of a point analysis in (a).

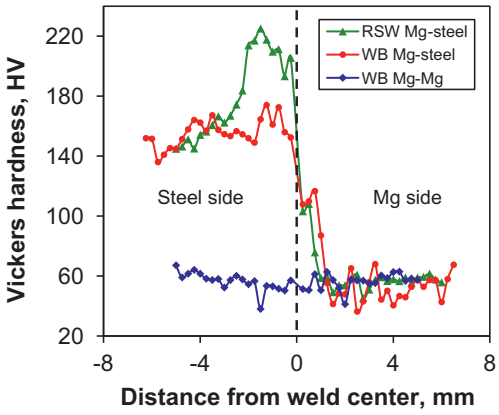

Fig. 8. Hardness profiles across the WB Mg/Mg similar joint, WB Mg/steel dissimilar joint, and RSW Mg/steel dissimilar joint.

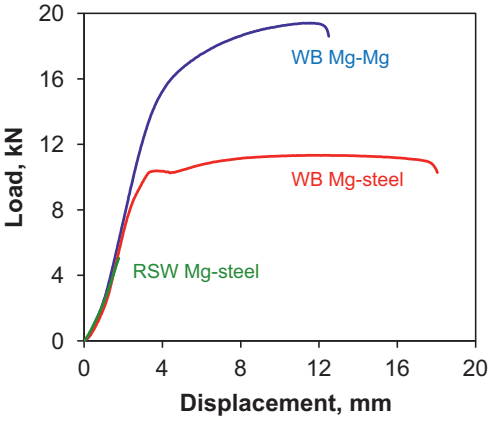

Fig. 9. Tensile load versus displacement for the WB Mg/Mg similar joint, WB Mg/steel dissimilar joint, and RSW Mg/steel dissimilar joint.

further higher than that of the RSW Mg/steel joint. While the maximum tensile shear load of the RSW Mg/steel joint decreased slightly with increasing crosshead speed, the maximum tensile shear load of both the WB Mg/Mg and WB Mg/steel joints increased slightly. All of the tensile shear tested samples showed an interfacial fracture mode (Fig. 2). To characterize more completely the tensile shear characteristics of the welded joints and better identify the effect of welding processes, energy absorption has been estimated, where the energy absorption is defined as the area below the load–displacement curve (Fig. 9). When the tensile shear remained continuous after reaching the maximum load without failure (i.e., in the cases of WB Mg/Mg and WB Mg/steel joints in the present study), the energy absorption is calculated corresponding to a 5% load drop relative to the maximum load. The evaluated results are plotted in Fig. 10(b). The energy absorption of both the WB Mg/Mg and WB Mg/steel joints was substantially higher than that

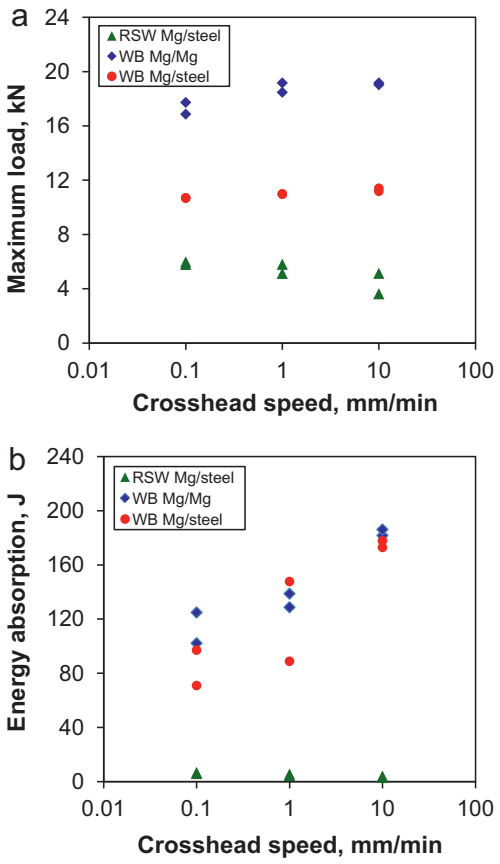

Fig. 10. (a) The maximum tensile shear load and (b) the energy absorption versus crosshead speed for the WB Mg/Mg similar joint, WB Mg/steel dissimilar joint, and RSW Mg/steel dissimilar joint.

of the RSW Mg/steel joint, while the energy absorption of the WB Mg/Mg joint was slightly higher than that of WB Mg/steel joint. Similar to the maximum shear load (Fig. 10(a)), the energy absorption of the RSW Mg/steel decreased with increasing strain rate (or crosshead speed). This was basically due to adiabatic heating during the tensile test [58,59]. On the other hand, the absorbed energy of WB Mg/Mg and WB Mg/steel joints increased to a greater extent with increasing crosshead speed. This reflects the beneficial role of weld adhesive, since the energy absorption capability is an important parameter in vehicle crashworthiness. There exists a direct relationship between the failure energy in the static tensile shear tests and impact tests. This implies that WB welding had a significantly higher impact resistance than RSW welding. Similar variation trend was also reported in [60–63]. For instance, Challita et al. [62] observed that the highest stress increased with increasing crosshead speed in the tensile test of the double-lap adhesively bonding. Goglio et al. [63] studied the effect of strain rate on the mechanical behavior of epoxy adhesives and observed that the maximum stress of the tested adhesive was very sensitive to the strain rate (i.e., increased with increasing strain rate). The addition of adhesive in the present WB joints would effectively promote the positive strain rate dependence. The significant improvement in both the maximum tensile shear load and energy absorption (Fig. 10(a) and (b)) suggests that the added adhesive played a predominant role in the joints. The superposition of adhesive bonding and spot welding led to the maximum load and especially the energy absorption increasing with increasing crosshead speed.

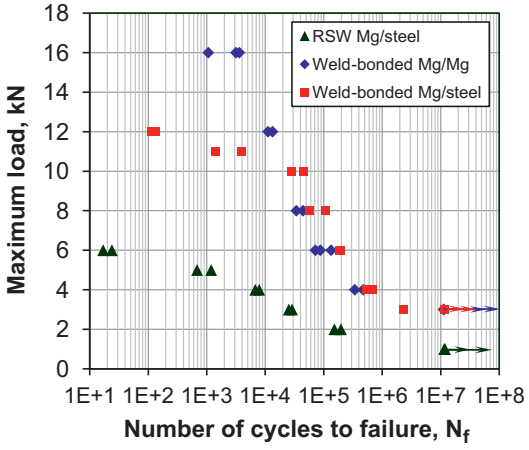

Fig. 11. S–N curves of the WB Mg/Mg similar joint, WB Mg/steel dissimilar joint, and RSW Mg/steel dissimilar joint tested at RT, $R = 0.2$, and a frequency of 50 Hz.

3.5. Fatigue strength and failure mode

Fatigue test results of RSW Mg/steel, WB Mg/Mg and WB Mg/steel joints obtained at RT, $R = 0.2$, and 50 Hz are plotted in Fig. 11. The fatigue life of both the WB Mg/Mg and WB Mg/steel joints was equivalent within the experimental scatter when the applied maximum cyclic load was below about 10 kN, which was much longer than that of the RSW Mg/steel joint at a given maximum cyclic load. Indeed, the fatigue strength (reflected by the maximum cyclic load in Fig. 11) at a given number of cycles to failure was about three times higher for the WB Mg/Mg and WB Mg/steel joints than for the RSW Mg/steel joint. For example, at a fatigue life of $\sim 1 \times 10^5$ cycles, it is seen that the fatigue strength of the WB Mg/Mg and WB Mg/steel joints was about three-fold higher than that of the RSW Mg/steel joint. The greatly improved fatigue resistance of the WB Mg/Mg and WB Mg/steel joints was primarily attributed to the weakening or elimination of stress concentration surrounding the weld nugget/button as a result of large bonded area and uniform stress distribution in the joint during fatigue tests. Similar results were reported in Refs. [61,64,65], where the fatigue life of the WB joint was longer than that of the RSW joint in the advanced high strength steels or aluminum alloy 5754-H40 as well. Therefore, the WB joints exhibited a significant improvement over the RSW joints. The equivalency of the S–N type of curves between the WB Mg/Mg similar joint and WB Mg/steel dissimilar joint when the maximum cyclic load was lower than ~10 kN in Fig. 11 indeed reflected the fatigue life of Mg base alloy itself, since the failure of all tested samples exclusively occurred in the base metal at the Mg side and normal to the loading direction, as shown in Fig. 12(a) and (b). In contrast, the failure of RSW Mg/steel joint occurred in the HAZ, i.e., the fatigue crack initiated from the HAZ and then propagated perpendicular to the loading direction at the maximum cyclic load of below 3 kN, as seen in Fig. 12(c), and in the mode of interfacial fracture at the maximum cyclic loads ranging in-between 3 and 6 kN (Fig. 12(d)). These observations indicated again that the WB joints were robust and durable without fatigue failure occurred at the joints even up to a maximum cyclic load of 10 kN, reflecting their high reliability and integrity. When the applied maximum cyclic load was above ~10 kN, while the WB Mg/Mg similar joints still exhibited a nearly linear change up to a maximum cyclic load as high as 16 kN, there existed an obvious inflection on the curve of WB Mg/steel dissimilar joints (Fig. 11), indicating a rapid reduction of fatigue life with increasing maximum cyclic load. This was due to the occurrence of large plastic deformation at the base metal of HSLA side, as shown in Fig. 13, because the maximum cyclic stress applied on the 0.7 mm thick

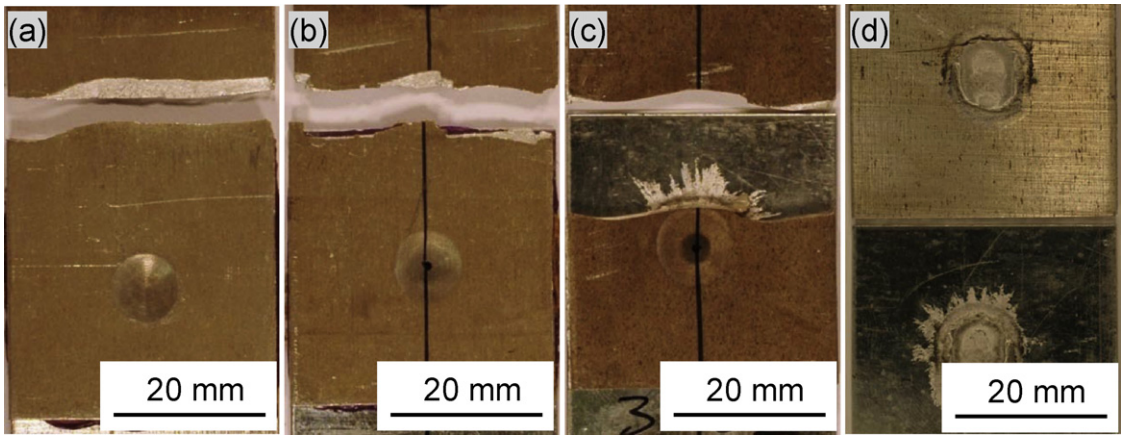

Fig. 12. Fatigue failure modes in (a) WB Mg/Mg joint at a maximum cyclic load of 12 kN, (b) WB Mg/steel joint at a maximum cyclic load of 10 kN, (c) RSW Mg/steel joint at a maximum cyclic load of 2 kN, and (d) RSW Mg/steel joint at a maximum cyclic load of 3 kN.

Fig. 13. Fatigue failure location of the WB Mg/steel joint at an applied maximum cyclic load of 12 kN.

base steel had exceeded its yield strength of HSLA. It should be pointed out that out of the four fatigue samples of WB Mg/steel dissimilar joints tested above the maximum cyclic load of 10 kN, three of them failed at the base metal of HSLA side due to the large plastic deformation shown in Fig. 13, while one of them failed in the mode of interfacial fracture which will be shown later. This implied that there was still remaining potential for the WB Mg/steel joint itself to endure a higher level of cyclic loading. To let such a WB Mg/steel dissimilar joint exert its full load-carrying capacity, either a thicker HSLA sheet or a higher grade of steel could be weld-bonded to the 2 mm thick AZ31 Mg alloy. Further studies in this aspect are needed. For the WB Mg/Mg joints, while the majority of samples tested at a maximum cyclic load below 16 kN failed in the base metal at the Mg side (Fig. 12(a)), partial button pullout

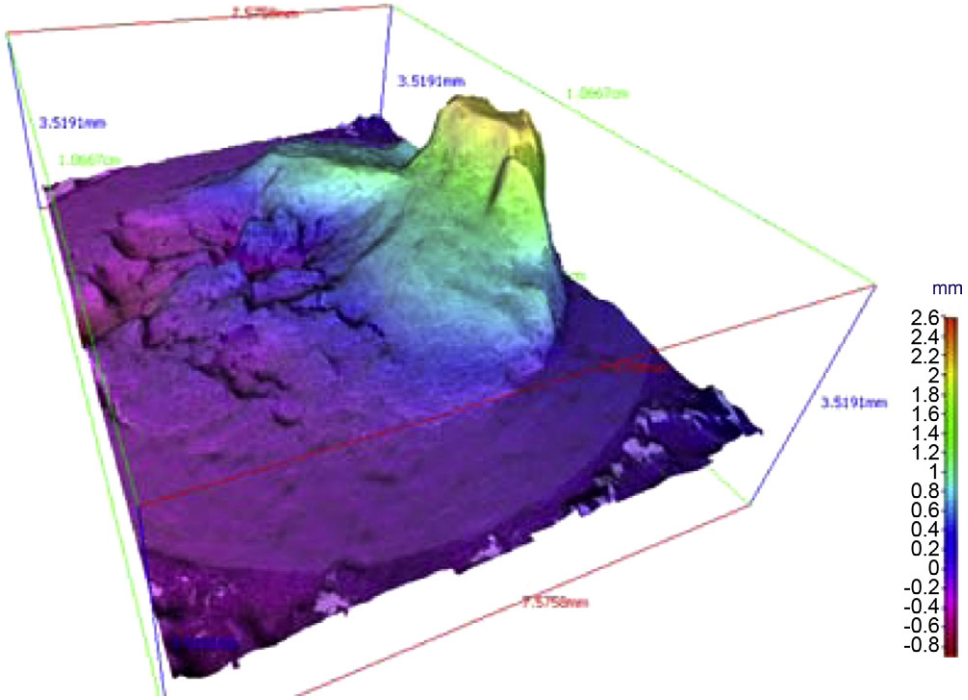

Fig. 14. A typical 3D SEM image showing the partial button pullout of the WB Mg/Mg similar joint after fatigue test at an applied cyclic maximum load of 16 kN.

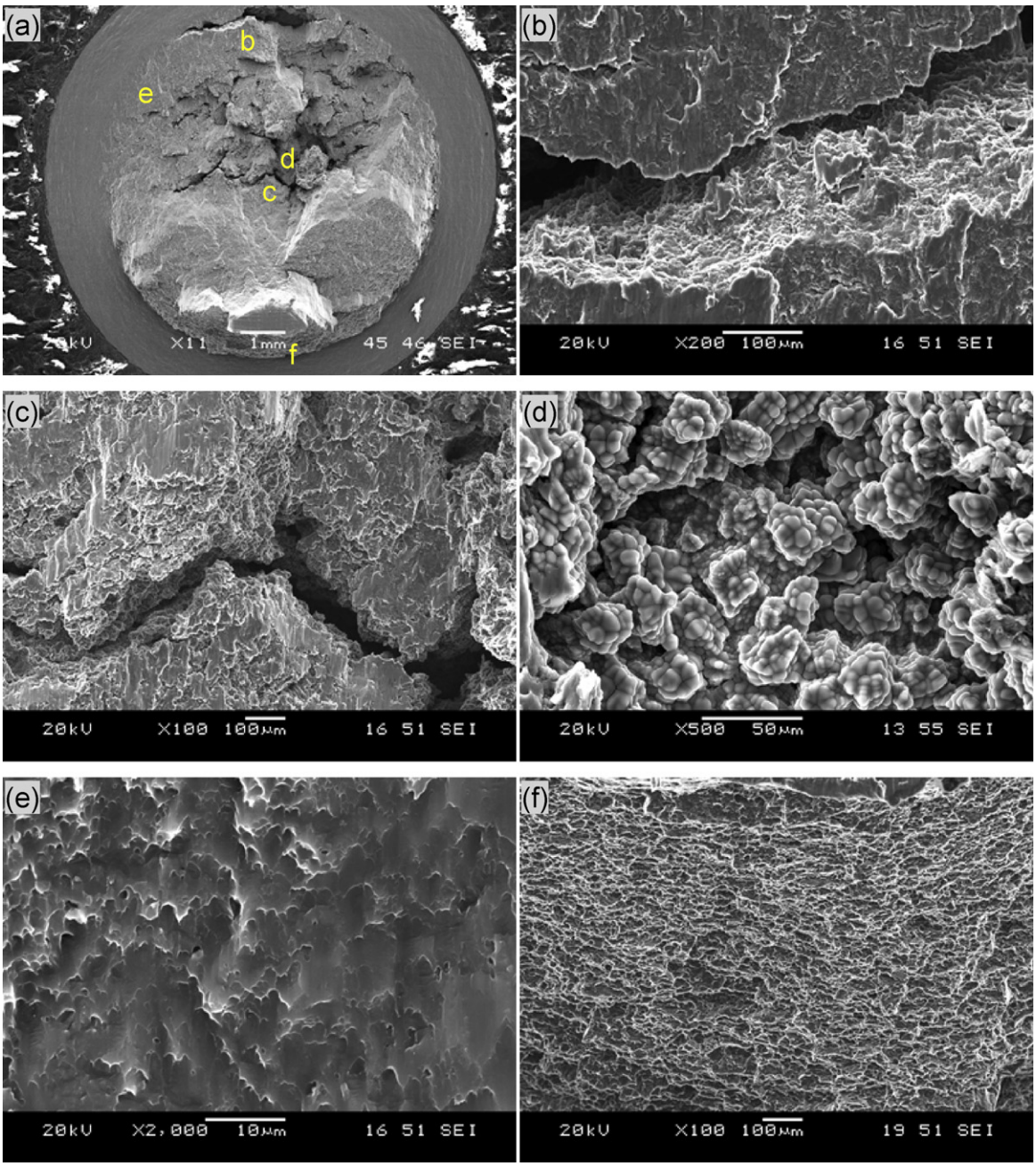

Fig. 15. SEM images of a fatigue fracture surface of a WB Mg/Mg similar joint tested at an applied cyclic maximum load of 16 kN: (a) overall view, (b) near the crack initiation site, (c) shrinkage crack in FZ, (d) shrinkage pore at a higher magnification, (e) facet-like shear deformation features, and (f) dimple features at the top of pull-out button.

failure was observed when the applied maximum cyclic load reached 16 kN, as seen from a three-dimensional image shown in Fig. 14. As mentioned above and shown in Fig. 12, the crack initiation sites for the WB Mg/steel joint and the RSW Mg/steel joint were different. While the RSW Mg/steel joints failed either due to crack initiation from the HAZ at the notch root and then crack propagation along the direction perpendicular to the loading direction (Fig. 12(c)) or in the mode of interfacial fracture (Fig. 12(d)), it should be noted that the notch root around the spot weld nugget was a place where the triaxial stresses reached the maximum value due to both the maximum shear stress and normal stress arising from the bending moment during lap shear tensile test [66,67]. Fatigue crack basically initiated at the edge of the overlapping/bonding area in the base metal of Mg side for the WB Mg/steel joints (Fig. 12(b)). This was understandable since a certain degree of stress concentration was still present at the edge of bonding area, although the stress concentration around the spot weld button was effectively reduced or eradicated by the adhesive bonding. Similar observations have also been reported in Refs. [68,69].

3.6. Fractography

To observe more details on the fracture surface, SEM images of the partial button pull-out failure of a WB Mg/Mg similar joint tested at a maximum cyclic load of 16 kN are shown in Fig. 15, where the cracks initiated from both sites “b” and “d” and grew across the weld nugget with increasing number of cycles. The feature for the crack initiation is shown in Fig. 15(b), which was fairly similar to that occurred in a typical RSW joint where the triaxial stresses reached the maximum value during the lap shear tensile

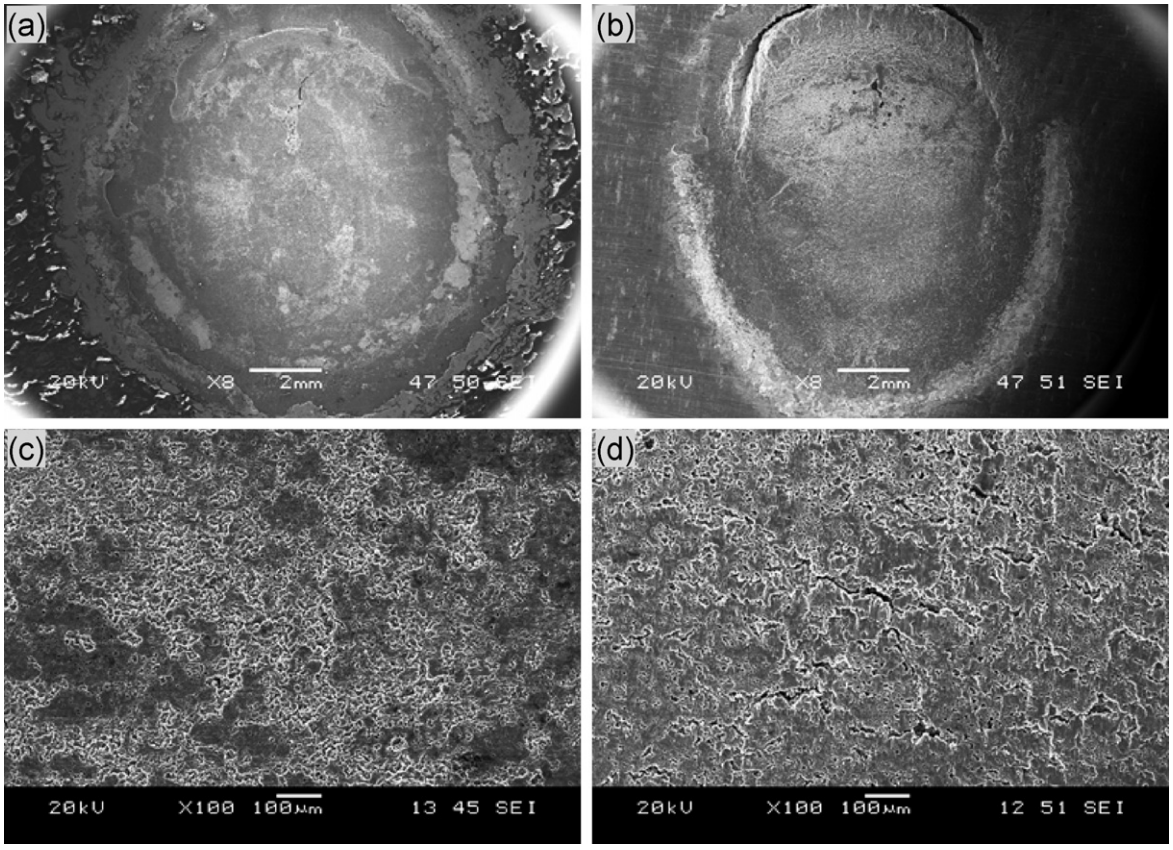

Fig. 16. SEM images of fatigue fracture surfaces of the WB Mg/steel and RSW Mg/steel dissimilar joints taken from the Mg side: (a) interfacial fracture surface of the WB Mg/steel joint tested at an applied cyclic maximum load of 11 kN, (b) interfacial fracture surface of the RSW Mg/steel joint tested at an applied cyclic maximum load of 5 kN, (c) fusion zone of the WB Mg/steel joint, and (d) fusion zone of the RSW Mg/steel joint.

tests. In addition, the internal shrinkage cracks and porosity in the weld nugget were also observed on the fractograph (Fig. 15(c and d)). Fatigue crack could be readily developed by growing and coalescing these shrinkage cracks and cavities located in the middle of the spot weld nugget, where the irregular shape of the cavities was very conducive to crack initiation and propagation with little plastic deformation. Fig. 15(d) shows clearly the dendritic structure in a cavity. The region in the cavity contained dendrite lobes, which existed as a "free surface" within the cavity after available liquid metal solidified. This feature might have been caused by a lack of molten metal within the cavity [23,65,67]. The typical crack propagation zone is shown in Fig. 15(c) for area "c" at a lower magnification and in Fig. 15(e) for area "e" with elliptical shear deformation characteristics. The dimple features in Fig. 15(f) indicated that the localized tensile stress appeared at the top of button pull-out part (Fig. 15(a)).

Fig. 16 presents SEM images of fatigue fracture surfaces of the WB Mg/steel and RSW Mg/steel dissimilar joints failed in the mode of interfacial fracture. At the Mg side of the WB Mg/steel joint (Fig. 16(a)) the overall fracture surface appeared smoother than that of the RSW Mg/steel joint (Fig. 16(b)). This was likely due to the presence of additional intermetallic compound of Mg_7Zn_3, as identified via XRD (Figs. 6(c) and 7). As mentioned earlier, in the WB Mg/steel joints tested above a maximum cyclic load of 10 kN (Fig. 11), while three samples failed at the base metal of HSLA side due to the large plastic deformation (Fig. 13), one sample failed in the mode of interfacial fracture (Fig. 16(a)). This was related to the presence of a visible initial shrinkage crack of ~1.5 mm long located near the top of the joint where the maximum stress also occurred (Fig. 16(a)), thus causing premature fatigue crack initiation from this location in this specific specimen. In view of the absence of interfacial failure in all other samples tested over a wide range of maximum cyclic loads from 3 kN to 12 kN (i.e., three samples above 10 kN and all other samples at or below 10 kN, as shown in Fig. 11), no serious defects in the weld nugget of the WB Mg/steel dissimilar joints would be expected. Indeed, by comparing the fusion zone of the WB Mg/steel joint with that of RSW Mg/steel joint in Fig. 16(c and d), smaller shrinkage cracks and cavities occurred more frequently in the RSW Mg/steel joint, which corresponded well to the cross-sectional observations shown in Figs. 3(b) and 4(b). This suggests that, despite the formation of additional intermetallic compound of Mg_7Zn_3, the lower cooling rate in the WB Mg/steel joints could generally reduce the tendency for the formation of shrinkage cracks and cavities, thus leading to improved quality of joints, in addition to the prevalent bonding role in reducing or eliminating the stress concentration around the spot weld nugget.

4. Conclusions

In this study the microstructures and mechanical properties of similar joints of WB Mg/Mg and dissimilar joints of WB Mg/steel and RSW Mg/steel were evaluated. The applied adhesive layer in WB Mg/Mg and WB Mg/steel welding had a significant influence on the microstructure and mechanical properties. The following conclusions can be drawn:

1. In the WB Mg/Mg similar joint, typical equiaxed dendritic and divorced eutectic structures formed in the fusion zone (FZ). No columnar dendritic structures near the fusion boundary were observed. This indicated that the applied adhesive layer reduced the temperature gradient and promoted columnar-to-equiaxed

transition during the weld-bonding process. The hardness across the WB Mg/Mg similar joint remained basically constant.

2. In the dissimilar joints of RSW and WB Mg/steel, FZ appeared only at the Mg side, consisting of equiaxed dendrites adjacent to the steel, and columnar dendrites near the fusion boundary. Compared with the RSW Mg/steel joint, the lower cooling rate in the WB Mg/steel joint tended to impede the presence of shrinkage cracks and cavities. At the steel side the microstructure did not change in the WB Mg/steel joint due to the lower cooling rate while it changed from polygonal ferrite to a mixture of lath martensite, bainite, pearlite and retained austenite, leading to a significant increase in the microhardness in the RSW Mg/steel joint.
3. X-ray diffraction revealed the formation of $MgZn_2$ in the RSW Mg/steel joint due to the presence of zinc coating on the hot-dip galvanized HSLA steel. The applied adhesive layer led to the occurrence of both $MgZn_2$ and Mg_7Zn_3 in the WB Mg/steel joint. This was due to the fact that the lower cooling rate in the weld bonding process equivalently increased diffusion time and thus promoted the formation of Mg_7Zn_3.
4. Tensile shear tests showed that the maximum tensile shear load was the highest for the WB Mg/Mg joint and the lowest for the RSW Mg/steel joint, with the values of the WB Mg/steel joint lying in-between them. However, the energy absorption of both WB Mg/Mg and WB Mg/steel joints was equivalent, which was substantially higher than that of the RSW Mg/steel joint.
5. While the maximum tensile shear load and energy absorption decreased slightly with increasing crosshead speed (or strain rate) in the RSW Mg/steel joint, they increased with increasing strain rate in both WB joints of Mg/Mg and Mg/steel. This reflected a beneficial role of weld adhesive in enhancing the energy absorption capacity in vehicle crashworthiness.
6. Fatigue life of both the WB Mg/Mg and WB Mg/steel joints was equivalent when the applied maximum cyclic load was below ~10 kN, which was much longer than that of the RSW Mg/steel joint. The fatigue strength at a given number of cycles was about three times higher for the WB Mg/Mg and WB Mg/steel joints than for the RSW Mg/steel joint. This was primarily attributed to the weakened stress concentration around the spot weld nugget as a result of large bonded area and more uniform stress distribution in the joint.
7. In the RSW Mg/steel joint fatigue crack initiated from the HAZ at the notch root and propagated perpendicular to the loading direction at the maximum cyclic load below 3 kN, and fatigue failure occurred in the mode of interfacial fracture at the maximum cyclic load above 3 kN. The failure of both WB Mg/Mg and WB Mg/steel joints basically occurred in the base metal at the Mg side and normal to the loading direction at a maximum cyclic load below ~10 kN, above which plastic deformation and final failure occurred mostly at the base metal of steel side in the WB Mg/steel joint as well as partial button pull-out occurred in the WB Mg/Mg joint.

Acknowledgments

The authors would like to thank the Natural Sciences and Engineering Research Council of Canada (NSERC) and AUTO21 Network of Centers of Excellence for providing financial support. This investigation involves part of Canada-China-USA Collaborative Research Project on the Magnesium Front End Research and Development (MFERD). The authors also thank General Motors Research and Development Center for the supply of test materials and POSCO/RIST for the support. One of the authors (D.L. Chen) is grateful for the financial support by the Premier's Research Excellence Award (PREA), NSERC-Discovery Accelerator Supplement (DAS) Award, Canada Foundation for Innovation (CFI), and Ryerson Research Chair (RRC) program. The assistance of Q. Li, A. Machin, J. Amankrah, and R. Churaman in performing the experiments is gratefully acknowledged. The authors also thank Dr. X. Cao, Dr. S. Xu, Dr. K. Sadayappan, Dr. M.S. Kozdras, Dr. J. Jackman, Professor N. Atalla, Professor S. Lambert, Professor H. Jahed, Professor Y.S. Yang, Professor M.F. Horstemeyer, Professor B. Jordon, Professor J. Allison, Dr. A.A. Luo, Mr. R. Osborne, Mr. J.F. Quinn, Dr. X.M. Su, and Mr. L. Zhang for the helpful discussion.

References

[1] Q. Schiermeier, Nature 470 (2011) 316.
[2] P. Pall, T. Aina, D.A. Stone, P.A. Stott, T. Nozawa, A.G.J. Hilberts, D. Lohmann, M.R. Allen, Nature 470 (2011) 382–385.
[3] M. Wise, K. Calvin, A. Thomson, L. Clarke, B. Bond-Lamberty, R. Sands, S.J. Smith, A. Janetos, J. Edmonds, Science 324 (2009) 1183–1186.
[4] L.R. Kump, Nature 419 (2002) 188–190.
[5] G.S. Cole, A.M. Sherman, Mater. Charact. 35 (1995) 3–9.
[6] H. Kang, I. Accorsi, B. Patel, E. Pakalnins, Procedia Eng. 2 (2010) 129–138.
[7] H.Y. Wang, L.M. Liu, Z.Y. Jia, J. Mater. Sci. 46 (2011) 5534–5540.
[8] R. Braun, Mater. Sci. Eng. A 426 (2006) 250–262.
[9] H. Friedrich, S. Schumann, J. Mater. Process. Technol. 117 (2001) 276–281.
[10] B.L. Mordike, T. Ebert, Mater. Sci. Eng. A 302 (2001) 37–45.
[11] T.M. Pollock, Science 328 (2010) 986–987.
[12] S.J. Liang, H.F. Sun, Z.Y. Liu, E. Wang, J. Alloys Compd. 472 (2009) 127–132.
[13] G.B. Hamu, D. Eliezer, L. Wagner, J. Alloys Compd. 468 (2009) 222–229.
[14] Y.R. Wang, Z.H. Mo, J.C. Feng, Z.D. Zhang, Sci. Technol. Weld. Join. 12 (2007) 641–646.
[15] J.B. Jiang, Z.D. Zhang, J. Alloys Compd. 466 (2008) 368–372.
[16] M.S. Khan, S.D. Bhole, D.L. Chen, G. Boudreau, E. Biro, J.V. Deventer, Can. Metall. Quart. 48 (2009) 303–310.
[17] K. Prasad, D.K. Dwivedi, Int. J. Adv. Manuf. Technol. 36 (2008) 475–483.
[18] B.H. Chang, Y.W. Shi, S.J. Dong, J. Mater. Process. Technol. 100 (2000) 171–178.
[19] V.M. Goncalves, P.A.F. Martins, Mater. Manuf. Process. 21 (2006) 774–778.
[20] I.O. Santos, W. Zhang, V.M. Goncalves, N. Bay, P.A.F. Martins, Int. J. Mach. Tools Manuf. 44 (2004) 1431–1439.
[21] A. Higgins, Int. J. Adhes. Adhes. 20 (2000) 367–376.
[22] L.M. Liu, J.B. Jiang, IEEE Trans. Plasma Sci. 39 (2011) 581–586.
[23] S.M.H. Darwish, A. Ghanya, J. Mater. Process. Technol. 105 (2000) 221–229.
[24] B. Lang, D.Q. Sun, G.Z. Li, X.F. Qin, Sci. Technol. Weld. Join. 13 (2008) 698–704.
[25] J. Mortimer, Ind. Robot 31 (2004) 423–428.
[26] J.F. Norton, Sheet Met. Ind. 11 (1981) 902–904.
[27] S. Barbagallo, H.I. Laukli, O. Lohne, E. Cerri, J. Alloys Compd. 378 (2004) 226–232.
[28] I.P. Moreno, T.K. Nandy, J.W. Jones, J.E. Allison, T.M. Pollock, Scripta Mater. 45 (2001) 1423–1429.
[29] J. Cai, G.C. Ma, Z. Liu, H.F. Zhang, Z.Q. Hu, J. Alloys Compd. 422 (2006) 92–96.
[30] S.M. Chowdhury, D.L. Chen, S.D. Bhole, X. Cao, E. Powidajkoc, D.C. Weckman, Y. Zhou, Mater. Sci. Eng. A 527 (2010) 2951–2961.
[31] S.M. Chowdhury, D.L. Chen, S.D. Bhole, E. Powidajko, D.C. Weckman, Y. Zhou, Metall. Mater. Trans. A 42A (2011) 1974–1989.
[32] L. Xiao, L. Liu, Y. Zhou, S. Esmaeili, Metall. Mater. Trans. A 41A (2010) 1511–1522.
[33] L. Liu, L. Xiao, J.C. Feng, Y.H. Tian, S.Q. Zhou, Y. Zhou, Metall. Mater. Trans. A 41A (2010) 2642–2650.
[34] M.H. Burden, J.D. Hunt, Matell. Trans. A 6A (1975) 240–241.
[35] S. Kou, Welding Metallurgy, Wiley-Interscience Publication, New York, 1987.
[36] Y.S. Zhang, H.T. Sun, G.L. Chen, X.M. Lai, Proc. IMechE B 223 (2009) 1341–1350.
[37] D.Q. Sun, B. Lang, D.X. Sun, J.B. Li, Mater. Sci. Eng. A 460–461 (2007) 494–498.
[38] B. Lang, D.Q. Sun, Z.Z. Xuan, X.F. Qin, ISIJ Int. 48 (2008) 77–82.
[39] Y.R. Wang, Z.D. Zhang, Trans. China Weld. Inst. 27 (2006) 9–12.
[40] J. Senkara, H. Zhang, S.J. Hu, Weld. J. 4 (2004) 123–132.
[41] Y.R. Wang, J.C. Feng, Z.D. Zhang, Sci. Technol. Weld. Join. 11 (2006) 555–560.
[42] L.C. Burmeister, Convective Heat Transfer, 2nd ed., John Wiley & Sons, Inc., Hoboken, 1993.
[43] E.W. Kim, T.W. Eagar, Weld. Res. Suppl. 8 (1989) 303–312.
[44] V.K. Patel, S.D. Bhole, D.L. Chen, Scripta Mater. 65 (2011) 911–914.
[45] T. Loulou, J.P. Bardon, Exp. Heat Transfer 14 (2001) 251–264.
[46] S.W. Thompson, D.J. Colvin, G. Krauss, Metall. Mater. Trans. A 27A (1996) 1557–1571.
[47] W.B. Lee, S.G. Hong, C.G. Park, S.H. Park, Metall. Mater. Trans. A 33A (2002) 1689–1698.
[48] M.S. Khan, S.D. Bhole, D.L. Chen, E. Biro, G. Boudreau, J.V. Deventer, Sci. Technol. Weld. Join. 14 (2009) 616–625.
[49] J.E. Gould, S.P. Khurana, T. Li, Weld. J. 85 (2006) 111–116.
[50] L. Liu, L. Xiao, J.C. Feng, Y.H. Tian, S.Q. Zhou, Y. Zhou, Metall. Mater. Trans. A 41A (2010) 2651–2661.
[51] Z. Yang, T. Derboy, Metall. Trans. B 30B (1999) 483–493.
[52] A.A. Nayeb-Hashemi, J.B. Clark, Phase Diagrams of Binary Magnesium Alloys, ASM International, Metals Park, 1988.
[53] M.M. Wu, L. Wen, B.Y. Tang, L.M. Peng, W.J. Ding, J. Alloys Compd. 506 (2010) 412–417.
[54] A.N. Alhazaa, T.I. Khan, J. Alloys Compd. 494 (2010) 351–358.

[55] X.Q. Zeng, Y. Zhang, C. Lu, W.J. Ding, Y.X. Wang, Y.P. Zhu, J. Alloys Compd. 395 (2005) 213–219.
[56] Z.H. Wu, G. Song, Mater. Res. Innov. 14 (2010) 160–164.
[57] Z.P. Luo, S.Q. Zhang, Y.L. Tang, D.S. Zhao, Scripta Metall. Mater. 32 (1995) 1411–1416.
[58] G.E. Dieter, Mechanical Metallurgy, 3rd ed., Mcgraw-Hill, New York, 1986.
[59] A.E. Domiaty, J. Mater. Process. Technol. 32 (1992) 243–251.
[60] M. Pouranvari, A. Abedi, P. Marashi, M. Goodarzi, Sci. Technol. Weld. Join. 13 (2008) 39–43.
[61] G. Weber, H. Thommes, H. Gaul, O. Hahn, M. Rethmeier, Mat.-wiss. u.Werkstofftech. 41 (2010) 931–939.
[62] G. Challita, R. Othman, P. Casari, K. Khalil, Int. J. Adhes. Adhes. 31 (2011) 146–153.
[63] L. Goglio, M. Peroni, M. Rossetto, Key Eng. Mater. 347 (2007) 671–676.
[64] X. Long, S.K. Khanna, Sci. Technol. Weld. Join. 13 (2008) 241–247.
[65] P.C. Wang, S.K. Chisholm, G. Banas, F.V. Lawrence, Weld. J. 2 (1995) 41–47.
[66] Y.J. Chao, J. Eng. Mater.-Trans. ASME 125 (2003) 125–132.
[67] C. Ma, D.L. Chen, S.D. Bhole, G. Boudreau, A. Lee, E. Biro, Mater. Sci. Eng. A 485 (2008) 334–346.
[68] A. Al-Samhan, S.M.H. Darwish, Int. J. Adhes. Adhes. 23 (2003) 23–28.
[69] S.M. Darwish, J. Mater. Process. Technol. 134 (2003) 352–362.